

A MOLECULAR LINE SCAN IN THE HUBBLE DEEP FIELD NORTH: CONSTRAINTS ON THE CO LUMINOSITY FUNCTION AND THE COSMIC H₂ DENSITY

WALTER F.¹, DECARLI R.¹, SARGENT M.², CARILLI C.³, DICKINSON M.⁴, RIECHERS D.⁵, ELLIS R.⁶, STARK D.⁷, WEINER B.⁷, ARAVENA M.^{8,9}, BELL E.¹⁰, BERTOLDI F.¹¹, COX P.¹², DA CUNHA E.¹, DADDI E.⁴, DOWNES D.¹², LENTATI L.¹³, MAIOLINO R.¹³, MENTEN K.M.¹⁴, NERI R.¹², RIX H.-W.¹, WEISS A.¹⁴

Accepted for publication in ApJ

ABSTRACT

We present direct constraints on the CO luminosity function at high redshift and the resulting cosmic evolution of the molecular gas density, $\rho_{\text{H}_2}(z)$, based on a blind molecular line scan in the Hubble Deep Field North (HDF-N) using the IRAM Plateau de Bure Interferometer. Our line scan of the entire 3 mm window (79–115 GHz) covers a cosmic volume of $\sim 7000 \text{ Mpc}^3$, and redshift ranges $z < 0.45$, $1.01 < z < 1.89$ and $z > 2$. We use the rich multiwavelength and spectroscopic database of the HDF-N to derive some of the best constraints on CO luminosities in high redshift galaxies to date. We combine the blind CO detections in our molecular line scan (presented in a companion paper) with stacked CO limits from galaxies with available spectroscopic redshifts (slit or mask spectroscopy from Keck and grism spectroscopy from HST) to give first blind constraints on high- z CO luminosity functions and the cosmic evolution of the H₂ mass density $\rho_{\text{H}_2}(z)$ out to redshifts $z \sim 3$. A comparison to empirical predictions of $\rho_{\text{H}_2}(z)$ shows that the securely detected sources in our molecular line scan already provide significant contributions to the predicted $\rho_{\text{H}_2}(z)$ in the redshift bins $\langle z \rangle \sim 1.5$ and $\langle z \rangle \sim 2.7$. Accounting for galaxies with CO luminosities that are not probed by our observations results in cosmic molecular gas densities $\rho_{\text{H}_2}(z)$ that are higher than current predictions. We note however that the current uncertainties (in particular the luminosity limits, number of detections, as well as cosmic volume probed) are significant, a situation that is about to change with the emerging ALMA observatory.

Subject headings: galaxies: formation — cosmology: observations — infrared: galaxies — galaxies: evolution

1. INTRODUCTION

The last decade has seen impressive advances in our understanding of galaxy formation and evolution based on deep field studies at various wavelengths. In particular, the cosmic history of star formation, and the build up of stellar mass as a function of galaxy type and mass, have

been well quantified, starting within 1 Gyr of the Big Bang. It has been shown that the comoving cosmic star formation rate density rose gradually from early epochs (at least $z \sim 6-8$) to a peak level between $z \sim 3$ and 1, after which it dropped by an order of magnitude towards the present (Hopkins & Beacom 2006, Bouwens et al. 2010). The build-up of stellar mass (i.e. the temporal integral) follows this evolution (Ilbert et al. 2009; Bell et al. 2007). The redshift range $z \sim 1-3$ constitutes the ‘epoch of galaxy assembly’, when roughly half the stars in the Universe formed.

While progress in deep field studies has been impressive, current knowledge of the formation of the general galaxy population is based almost exclusively on optical, near-IR and cm-radio deep field surveys of stars, star formation, and ionized gas. For example, Lyman Break selected samples have revealed a major population of star-forming galaxies at $z \sim 3$ (e.g., Steidel et al. 2004). Likewise, magnitude-selected samples (e.g., Le Fèvre et al. 2005, Lilly et al. 2007) provide a census of the star-forming population based on UV/optical flux rather than color. Radio-selected sources provide estimates of dust-unbiased star formation rates (e.g., Cowie et al. 2004, Dunne et al. 2009, Karim et al. 2011).

The molecular gas content is the cause of the cosmic star formation history. However, observations of the gas content have to date been limited to follow-up studies of galaxies that are pre-selected from optical/NIR deep surveys (or, in the extreme cases of quasar host galaxies and sub-millimeter galaxies, through selection in the sub-millimeter continuum, Carilli & Walter 2013). In all

¹ Max-Planck Institut für Astronomie, Königstuhl 17, D-69117, Heidelberg, Germany. E-mail: walter@mpia.de

² Laboratoire AIM, CEA/DSM-CNRS-Université Paris Diderot, Irfu/Service d’Astrophysique, CEA Saclay, Orme des Merisiers, 91191 Gif-sur-Yvette cedex, France

³ NRAO, Pete V. Domenici Array Science Center, P.O. Box O, Socorro, NM, 87801, USA

⁴ National Optical Astronomy Observatory, 950 North Cherry Avenue, Tucson, Arizona 85719, USA

⁵ Cornell University, 220 Space Sciences Building, Ithaca, NY 14853, USA

⁶ Astronomy Department, California Institute of Technology, MC105-24, Pasadena, California 91125, USA

⁷ Steward Observatory, University of Arizona, 933 N. Cherry St., Tucson, AZ 85721, USA

⁸ European Southern Observatory, Alonso de Cordova 3107, Casilla 19001, Vitacura Santiago, Chile

⁹ Núcleo de Astronomía, Facultad de Ingeniería, Universidad Diego Portales, Av. Ejército 441, Santiago, Chile

¹⁰ Department of Astronomy, University of Michigan, 500 Church St., Ann Arbor, MI 48109, USA

¹¹ Argelander Institute for Astronomy, University of Bonn, Auf dem Hügel 71, 53121 Bonn, Germany

¹² IRAM, 300 rue de la piscine, F-38406 Saint-Martin d’Hères, France

¹³ Cavendish Laboratory, University of Cambridge, 19 J J Thomson Avenue, Cambridge CB3 0HE, UK

¹⁴ Max-Planck-Institut für Radioastronomie, Auf dem Hügel 69, 53121 Bonn, Germany

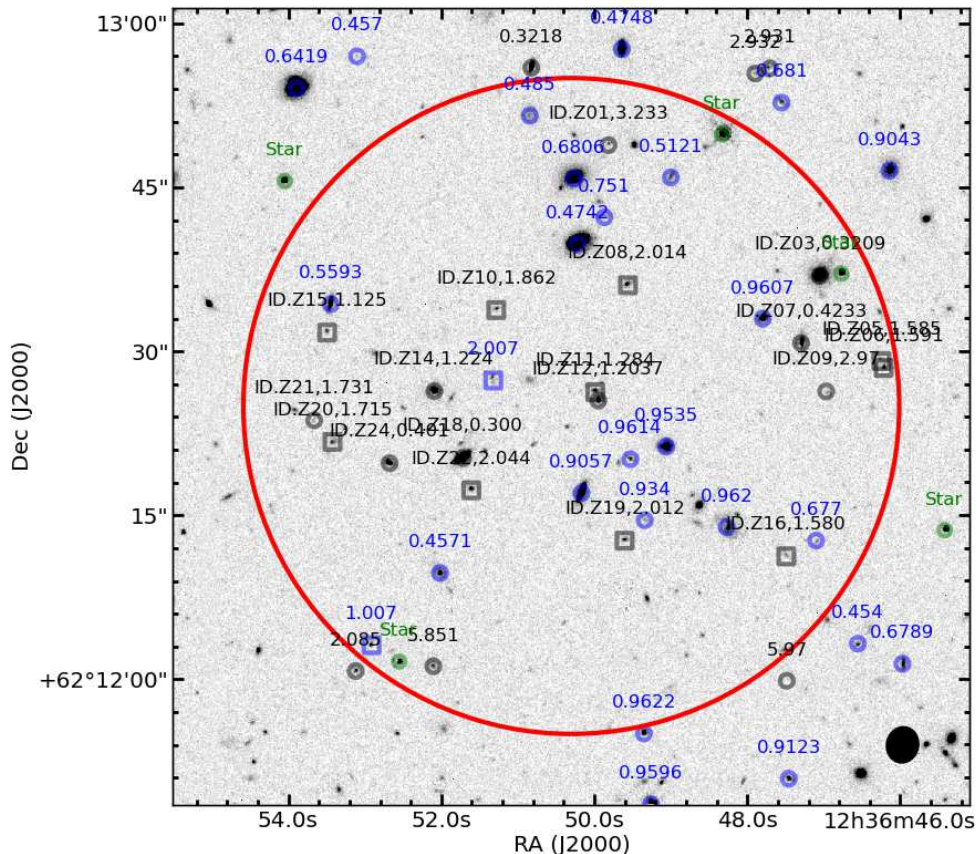


FIG. 1.— HST/WFC3 F160W ($1.6\mu\text{m}$) image from the CANDELS survey (Grogin et al. 2011; Koekemoer et al. 2011) of the region of the HDF-N covered by our line scan from the CANDELS survey. The red circle shows the primary beam FWHM of our observations at the intermediate frequency of our scan (97.25 GHz). The black ellipse in the bottom-right corner shows the synthesized beam of our observations. Galaxies are labeled with their redshift. Blue colors indicate redshifts that are not covered by the frequency coverage of our 3 mm scan (Tab. 1). Circles indicate ground-based redshifts and squares indicate slit-less (grism) redshifts (when both are available, only ground-based redshifts are shown). Green color indicates stars in the field. We show the spectroscopic completeness as a function of H -band magnitude in Fig. 2 and CO spectra towards all galaxies with redshift information in Fig. 3.

cases the selection is based on the star formation properties of a given galaxy.

In order to obtain an unbiased census of the molecular gas content in high- z galaxies, there is a clear need for a blind search of molecular gas down to mass limits characteristic of the normal star forming galaxy population, i.e., a molecular deep field. Such a molecular deep field has been out of reach using past instrumentation, both in terms of sensitivity and instantaneous bandwidth. However they are now becoming feasible, in particular given the unparalleled sensitivity of Atacama Large (Sub-)Millimeter Array (ALMA). We here present results based on a precursor program, using the IRAM Plateau de Bure Interferometer (PdBI), of the Hubble Deep Field North (HDF-N, Williams et al. 1996), that is discussed in detail in Decarli et al. (2013, hereafter D13). After a brief summary of the observations (Sec. 2) we discuss stacked molecular gas limits (based on galaxies with known spectroscopic redshifts, Sec. 3.1). Together with the ‘blind’ CO line detections from D13 (Sec. 3.2) these give first constraints on the redshift dependence of the CO luminosity function in the HDF-N and their implications for the cosmic evolution of the molecular gas content in galaxies (Sec. 4). A short summary and outlook is presented in Sec. 5. Throughout the paper we adopt a standard cosmology with $H_0 = 70 \text{ km s}^{-1}$

Mpc^{-1} , $\Omega_m = 0.3$ and $\Omega_\Lambda = 0.7$.

2. DATA

2.1. Complete frequency scan of the 3-mm band

We have observed the full 3-mm band of the PdBI ($\sim 79.7\text{--}114.8\text{GHz}$) to approximately uniform sensitivity, reaching an average noise of $\sim 0.3 \text{ mJy beam}^{-1}$ in a 90 km s^{-1} channel (pointing centre: $12:36:50.300 +62:12:25.00$). Observations were done in C-array configuration, resulting in an average beam size of $\sim 3''$, or $\sim 25 \text{ kpc}$ at redshifts $\gtrsim 1$. At this resolution we do not expect to spatially resolve high-redshift galaxies. The observational details are discussed in D13. Table 1 summarizes the redshift ranges probed by the different CO transitions covered by our scan and Fig. 1 shows the field covered by our observations. Table 1 also gives the cosmic volume probed by our observations. Here we take into account that the covered sky area, as defined by the primary beam, changes as a function of frequency.

2.2. Optical/NIR spectroscopy in the HDF-N

In our analysis we use available multiwavelength information of the galaxies in the HDF-N, in particular (spectroscopic) redshift estimates, to improve our sensitivity to search for CO emission.

The H -band selected catalogue by Dickinson et al.

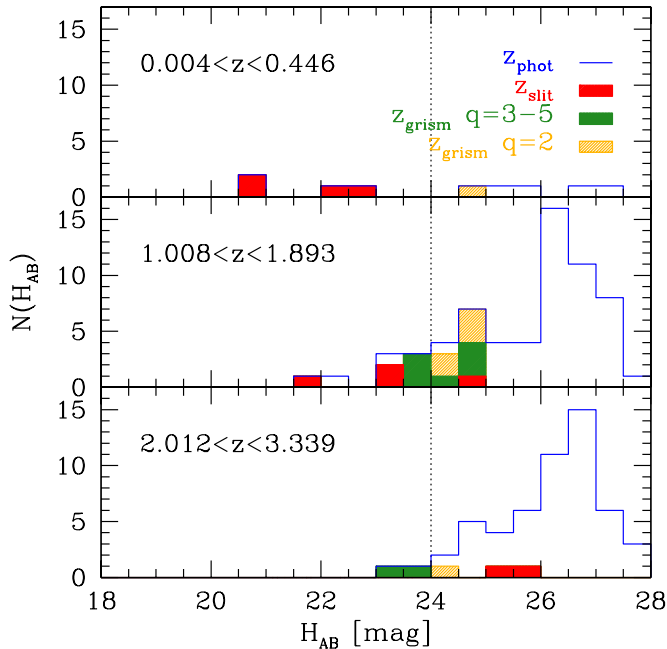


FIG. 2.— Histogram of number of galaxies covered in our line scan as a function of H -band magnitude (x-axis) and redshift bin (3 panels). The blue line shows the distribution of galaxies with photometric redshifts in each redshift bin (available for most of the galaxies in the field), whereas the colored regions indicate the availability of ground-based spectroscopic redshifts (red) and high-quality HST grism spectroscopy (green). Grism spectra with quality $q=2$ (yellow) are the least reliable and we do not use them for our analysis. Ground-based redshifts are preferred to HST grism ones, when both are available.

TABLE 1
REDSHIFT RANGE AND COSMIC VOLUME COVERED BY MOLECULAR LINE SCAN.

| line | z_{\min} | z_{\max} | $\langle z \rangle^a$ | Volume ^b Mpc ³ |
|---------|------------|------------|-----------------------|---|
| CO(1-0) | 0.0041 | 0.446 | 0.338 | 91.66 |
| CO(2-1) | 1.01 | 1.89 | 1.52 | 1442 |
| CO(3-2) | 2.01 | 3.34 | 2.75 | 2437 |
| CO(4-3) | 3.02 | 4.78 | 3.98 | 2966 |
| CO(5-4) | 4.02 | 6.23 | 5.21 | 3249 |

NOTE. —

^a Volume-averaged redshift of CO transition.

^b Cosmic comoving volume probed by redshift range. As sky area we use the frequency-dependent size of the PdBI primary beam ($\text{FWHM} = 55'' \times \frac{86}{\nu(\text{GHz})}$).

(2003), based on deep HST/NICMOS F160W photometry, lists 220 galaxies within $30''$ (i.e. roughly the size of the primary beam from the pointing center of our observations. Cowie et al. (2004) and Barger et al. (2008) provide spectroscopic redshifts for 15 of these. We add to this so far unpublished spectroscopic redshifts (based on Keck spectroscopy, Dickinson et al., in prep.) for an additional 8 galaxies up to $z=4$. One additional faint galaxy is included at $z=4.355$ – this redshift is based on one line (presumably Ly- α) and no continuum is seen in the spectrum (Stark et al. 2010). All spectroscopic redshifts based on ground observations are from the Keck telescope. In addition to these, we add secure grism-

TABLE 2
GALAXIES WITH GROUND-BASED OR HST GRISM-BASED REDSHIFTS COVERED BY MOLECULAR LINE SCAN.

| ID | RA (J2000.0) | Dec (J2000.0) | z_{spec} | z_{grism} | grism quality |
|--------|-----------------|------------------|-------------------|--------------------|---------------|
| (1) | (2) | (3) | (4) | (5) | (6) |
| ID.Z01 | 12:36:49.81 | +62:12:48.8 | 3.233 | | |
| ID.Z02 | 12:36:50.26 | +62:12:49.6 | | | |
| ID.Z03 | 12:36:47.04 | +62:12:36.9 | 0.3209 | [1.625] | 2 |
| ID.Z04 | 12:36:47.61 | +62:12:37.2 | | [0.321] | 2 |
| ID.Z05 | 12:36:46.24 | +62:12:29.1 | | [0.423] | 2 |
| ID.Z06 | 12:36:46.22 | +62:12:28.5 | | 1.585 | 3 |
| ID.Z07 | 12:36:47.28 | +62:12:30.7 | 0.4233 | 1.591 | 3 |
| ID.Z08 | 12:36:49.56 | +62:12:36.1 | | 2.014 | 3 |
| ID.Z09 | 12:36:46.94 | +62:12:26.1 | 2.970 | 3 | 3 |
| ID.Z10 | 12:36:51.28 | +62:12:33.8 | | 1.862 | 3 |
| ID.Z11 | 12:36:49.99 | +62:12:26.3 | | 1.284 | 3 |
| ID.Z12 | 12:36:49.95 | +62:12:25.5 | 1.204 | 1.205 | 5 |
| ID.Z13 | 12:36:50.35 | +62:12:23.0 | | [1.185] | 2 |
| ID.Z14 | 12:36:52.09 | +62:12:26.3 | 1.224 | 1.166 | 3 |
| ID.Z15 | 12:36:53.49 | +62:12:31.7 | | 1.125 | 3 |
| ID.Z16 | 12:36:47.49 | +62:12:11.2 | | 1.58 | 3 |
| ID.Z17 | 12:36:51.74 | +62:12:21.4 | | [2.713] | 2 |
| ID.Z18 | 12:36:51.71 | +62:12:20.2 | 0.300 | | |
| ID.Z19 | 12:36:49.60 | +62:12:12.7 | | 2.012 | 3 |
| ID.Z20 | 12:36:53.42 | +62:12:21.7 | | 1.715 | 4 |
| ID.Z21 | 12:36:53.66 | +62:12:23.7 | 1.731 | 1.739 | 3 |
| ID.Z22 | 12:36:51.61 | +62:12:17.3 | | 2.044 | 5 |
| ID.Z23 | 12:36:53.91 | +62:12:24.5 | | [1.797] | 2 |
| ID.Z24 | 12:36:52.67 | +62:12:19.8 | 0.401 | | |
| ID.Z25 | 12:36:48.80 | +62:12:02.1 | | [1.038] | 2 |
| ID.Z26 | 12:36:51.89 | +62:12:08.1 | | [1.144] | 2 |
| ID.Z27 | 12:36:50.48 | +62:12:50.4 | 4.345 | | |

NOTE. — Catalogue of the galaxies with ground-based or HST grism-based redshift (from optical/NIR observations) consistent with the CO redshift coverage of our line scan (Tab. 1). (1) Line ID. (2-3) Right ascension and declination (J2000). (4) Spectroscopic (ground-based) redshift from Cowie et al. (2004); Reddy et al. (2006); Barger et al. (2008); Stark et al. (2010). (5) Grism-based redshift from AGHAST (Weiner et al., in prep.). (6) Quality of the grism redshift (5: highest, 2: lowest; we consider only quality 3-5 in our analysis and have but the quality 2 redshifts in brackets).

based redshifts (based on the detection of emission lines) and lower-quality redshifts (e.g., based on absorption features or on the shape of the continuum emission) from the HST survey ‘A Grism H-Alpha Spectroscopic survey’ (AGHAST, Weiner et al., in prep.). A quality flag q is assigned to all grism-based redshifts in Tab. 2. Higher values ($q=3-5$) are associated with grism redshifts based on emission lines. $q=2$ values are associated with more uncertain redshifts, e.g., based on the shape of the continuum emission. Out of our complete spectroscopic set of 47 galaxies, 27 have a redshift that is covered by our scan (Tab. 1 and Fig. 1).

This final sample of 27 galaxies with redshifts covered by our frequency scan is listed in Tab. 2. These galaxies and their respective ID’s are marked by circles (ground-based redshift) and squares (slit-less HST grism redshifts) in Fig. 1. In Fig. 2 we show the spectroscopic completeness in the field as a function of H -band magnitude (to first order a measure of the stellar mass) for the redshift intervals covered by our molecular line scan. From this we conclude that we reach high spectroscopic completeness (i.e. $> 90\%$) down to H -band magnitudes of $H_{\text{AB}} < 24$ mag for all redshift bins. This corresponds to the following stellar masses in each redshift bin: $\langle z \rangle = 0.338$: $\sim 5.0 \times 10^7 M_{\odot}$, $\langle z \rangle = 1.52$: $\sim 3.3 \times 10^9 M_{\odot}$, $\langle z \rangle = 2.75$: $\sim 7.0 \times 10^9 M_{\odot}$ (da Cunha et al. 2013).

TABLE 3
STACKED CO LIMITS BASED ON THE AVAILABLE SPECTROSCOPIC REDSHIFT INFORMATION.

| line | $\langle z \rangle$ | # ^a | S _{CO} Jy km s ⁻¹ | L _{CO} 10 ⁶ L _⊙ | L' _{CO} 10 ⁹ K km s ⁻¹ pc ² | L' _{CO(1-0)} ^b 10 ⁹ K km s ⁻¹ pc ² | density ^c 10 ⁻³ Mpc ⁻³ |
|---------|---------------------|----------------|--|---|--|--|--|
| CO(1-0) | 0.338 | 4 | <0.177 | <0.034 | <0.68 | <0.68 | 43 |
| CO(2-1) | 1.52 | 10 | <0.174 | <2.1 | <5.2 | <5.91 | 6.9 |
| CO(3-2) | 2.75 | 5 | <0.443 | <22.0 | <17 | <34 | 2.1 |

NOTE. — All upper limits are 5σ . The CO(2-1) and CO(3-2) limits account for the higher uncertainties in the grism redshifts (see Sec. 3.1).

^a Number of galaxies in stack (from Tab. 2 and Fig. 2).

^b We have converted our high-J CO L'_{CO} luminosity limits to L'_{CO(1-0)} assuming L'_{CO(2-1)}/L'_{CO(1-0)}=0.84 and L'_{CO(3-2)}/L'_{CO(1-0)}=0.5 (Dannerbauer et al. 2009).

^c Volume density of sources in redshift bin using column 5 in Tab. 1.

3. ANALYSIS

We base our analysis on two measurements: (A) deep stacked CO limits based on the available optical/NIR spectroscopy (Sec. 3.1) and (B) the blind CO detections discussed in D13 (Sec. 3.2).

3.1. Stacked CO limits based on known spectroscopic redshifts

We here use the spectroscopic redshift information presented in Sec. 2.2 to aid in our search for CO emission, and to obtain a stacked CO limit in the galaxy samples. In Fig. 3 we show the spectra extracted at the pixel of the nominal positions of the galaxies with spectroscopic redshifts (Tab. 2), shifted to their respective redshifts; here we exclude sources that only have low-quality (quality 2) grism redshifts. All spectra have been corrected for primary beam attenuation, leading to different noise properties in the spectra. None of the spectra show convincing CO emission at the expected redshift. In our blind search for CO (D13) we report a candidate CO line emission for one of the sources shown in Fig. 3, ID.Z22, which is spatially consistent with the CO line candidate ID.19 and where the grism redshift matches the CO redshift perfectly (see detailed discussion in D13)¹⁵. We also note that one galaxy, ID.Z27 at $z=4.345$ (Stark et al. 2010), shows a tentative CO(4-3) line but we treat this as an upper limit in our analysis.

To stack the spectra, we first need to consider the accuracy of the available optical/NIR redshifts: The typical uncertainties of Keck spectroscopic redshifts $z \leq 1.6$ are of order few tens of km s^{-1} (Newman et al. 2012), and we consider these uncertainties negligible for our stacking, given the expected line widths of $\sim 300 \text{ km s}^{-1}$ (e.g., Carilli & Walter 2013). At higher redshifts, the uncertainties are higher (a few hundred km s^{-1}) due to various observational and astrophysical biases e.g., lack of bright nebular lines, such as [O III] or [O II], or rest frame UV features showing systematic offsets (e.g. Steidel et al. 2010). The average uncertainty in the grism redshifts is $\delta z/(1+z) \approx 0.0016$ (Weiner et al., in prep.). These higher uncertainties are related to poorer spectral resolution, confusion between spatial and spectral structure in slitless observations, and the intrinsic weakness of the lines.

For our stack we weight-average the primary-beam

¹⁵ For this source, we also show the spectrum that corresponds to the CO candidate ID.19 that is offset by 1.5" from the optical/NIR counterpart for the optical galaxy ID.Z22 in Fig. 3. See detailed discussion of CO candidate ID.19 in D13.

corrected spectra after realignment and rebinning (bottom panels of Fig. 3). Given the uncertainties in grism redshifts, we compute the stacked flux as the integral (and its uncertainties) of the stacked spectra over 1000 km s^{-1} (i.e., sufficient to encompass any CO emission within the typical redshift uncertainties). A tighter velocity range of 300 km s^{-1} was assumed for the lowest redshift bin, where all galaxies have a more accurate ground-based redshift. The final stacked upper limits for the CO fluxes and resulting luminosities are given in Tab. 3.

3.2. Blind CO detections from molecular line scan

In D13 we present a blind search for CO emission in the molecular line scan above a luminosity limit of $\sim 6 \times 10^9 \text{ K km s}^{-1} \text{ pc}^2$ (to first order irrespective of CO transition, see D13). 17 potential candidate lines are discussed in D13 and here we concentrate on the ones with quality flag 'high-quality' and 'secure', which leaves 13 sources. Two line candidates (ID.08 and ID.17) belong to the highly obscured galaxy HDF 850.1 at $z=5.183$ (Walter et al. 2012). This source has previously been selected as a sub-millimeter galaxy (and our field centre was chosen to include it) so we do not discuss it further here. There are two additional galaxies in the 'secure' list for which we are certain of their redshifts: ID.03 at $z=1.7844$ (redshift derived from three CO lines) and ID.19 at $z=2.0474$ (ID.Z22 in Tab. 2; coincident CO and grism redshift); in both cases the spectral energy distributions (SEDs) based on the available multi-wavelength photometry are in excellent agreement with the derived redshifts (D13).

Based on the available multi-wavelength information, D13 assigned each of the remaining line candidates a tentative redshift. We stress that we expect some of the line candidates to be spurious¹⁶, and consequently treat the number of candidate detections in each redshift bin as an upper limit. Dedicated follow-up observations in other CO transitions are needed to confirm the reality and redshifts of our candidate lines. We record the number of blind line detections and limiting magnitudes in each redshift bin in Tab. 4.

4. IMPLICATIONS

¹⁶ In D13 we have derived the number of likely spurious detections using simulated data cubes. We find 2 sources classified as 'high-quality/secure', i.e. with spectroscopic $S/N > 3.5$, that are false detections. If we assign one to each redshift bin this leads to a spurious fraction of 1/3 and 1/8 for the two highest redshift bins.

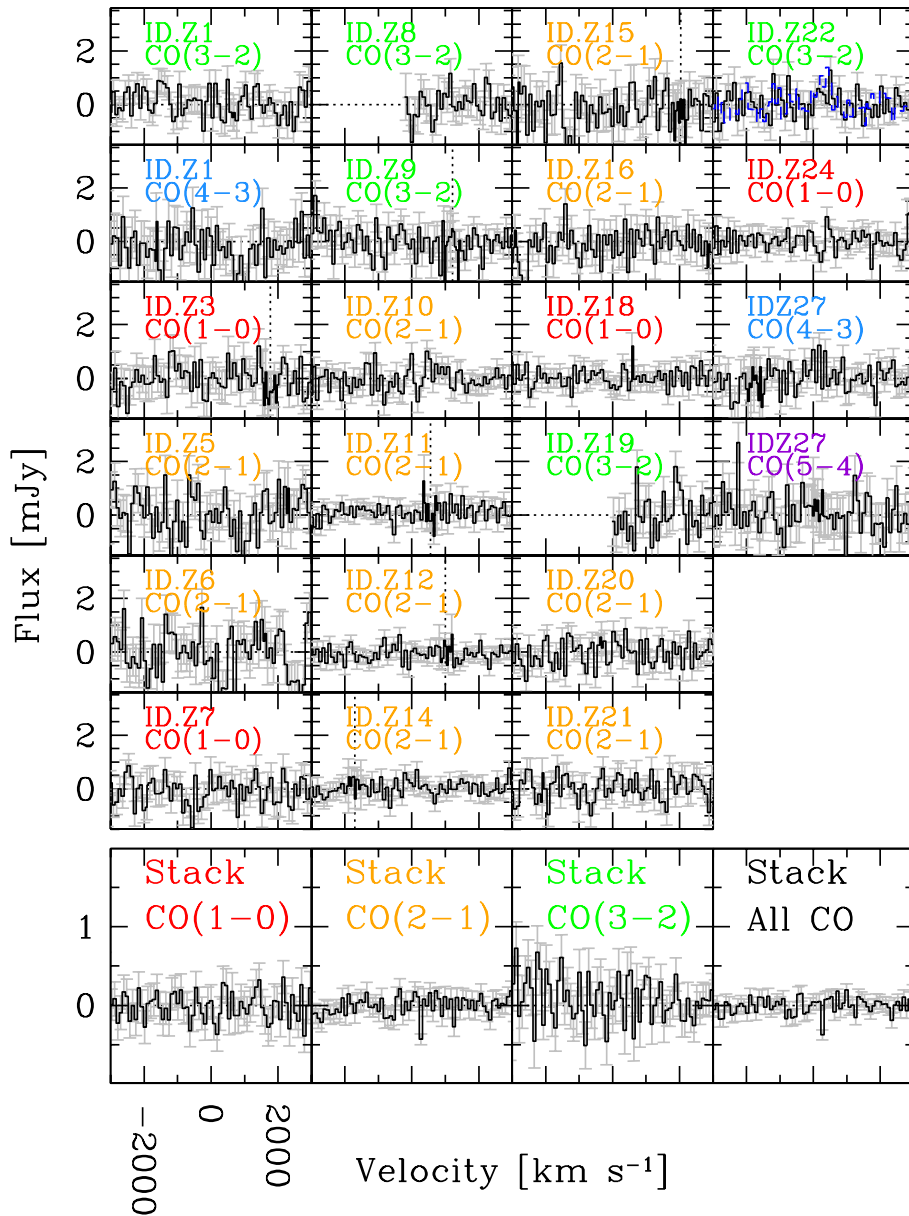


FIG. 3.— Spectra of the galaxies with high-quality spectroscopic redshifts falling within the range of redshifts our scan covered for various CO transitions (see Tabs. 1 and 2). Spectra are corrected for primary beam attenuation. No galaxy is individually detected at high significance. Vertical dashed lines indicate band edges in our scan (D13). ID.Z22 is spatially coincident with our blind CO detection ID.19 (see discussion in Sec. 3.1) and we show the spectrum of ID.19, extracted 1.5'' away from the optical positions, as a blue-dashed line for reference. The bottom panels show the stacked spectra for each transition and a stack of all CO emission. We note that ID.Z1 enters the latter stack twice as it has two lines in our scan.

Our molecular line scan in the HDF-N constitutes the first systematic blind search for CO emission down to a mass limit that is characteristic of galaxies that lie on the relatively tight ‘main sequence’ SFR- M_* relation (Daddi et al. 2007). Its cosmic volume is well defined and characterized through the ancillary multi-wavelength observations. In the following we discuss our constraints on the CO luminosity functions and the cosmic evolution of the cosmic molecular gas density $\rho_{\text{H}_2}(z)$ in the HDF-N.

4.1. Constraints on CO luminosity function

We now constrain the CO luminosity function at different redshifts based on our blind CO detections (Tab. 4,

Sec. 3.2). We compare our measurements to empirical predictions of the CO luminosity function. In Fig. 4 we show the CO(1-0) luminosity function in the three redshift bins covered by our line scan, as predicted by Sargent et al. (2013b) based on (1) the evolution of the stellar mass function of star-forming galaxies, (2) the redshift evolution of the specific SFR of main-sequence galaxies, (3) the distribution of main-sequence and star-bursting galaxies in the SFR- M_* -plane (Sargent et al. 2012), (4) distinct prescriptions of the star formation efficiency of main-sequence and star-bursting galaxies, and (5) a metallicity-dependent conversion factor α_{CO} .

In the same plot (Fig. 4) we also show the predictions

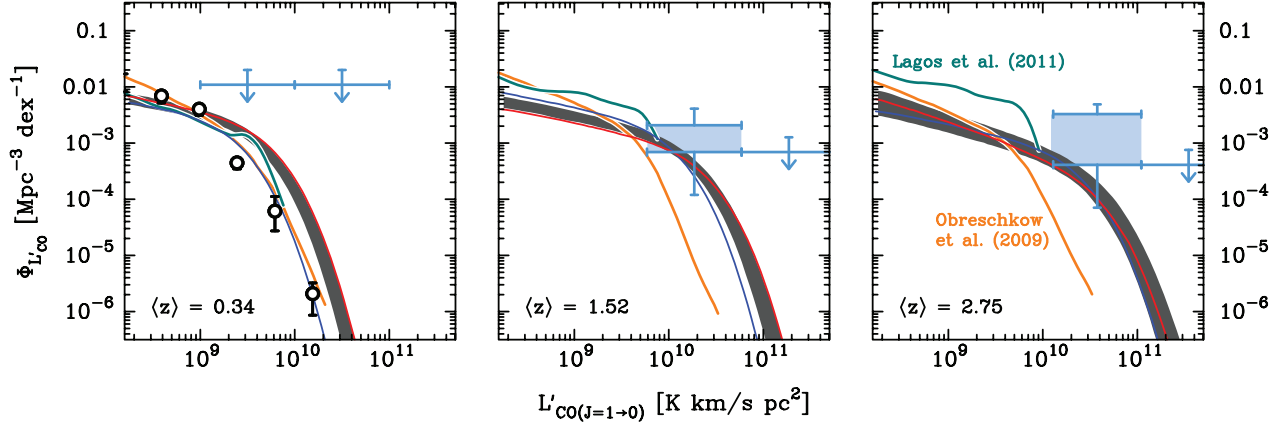


FIG. 4.— Comparison of our blind CO measurements with empirically derived CO luminosity functions from the literature. The grey shading shows the predictions by Sargent et al. (2013a) for the average (volume-weighted) redshift (Tab. 1) where the width indicates the 68% confidence region. As each redshift bin covers a significant range in redshifts we also show the median luminosity function for the lowest and highest redshift in the respective redshift bin (red and blue curve, here the 68% confidence region is not shown). Also shown are models for the evolution of the CO luminosity function based on semi-analytical cosmological models plus ‘recipes’ to relate gas mass to CO luminosity (Lagos et al. 2011 and Obreschkow et al. 2009a,b). In the left panel the observational constraints on the local ($z=0$) CO luminosity functions reported in Kereš et al. (2003) are also shown as data points (small circles). The blue-shaded regions shows the constraints derived from our blind detections (Tab. 4, Secs. 3.2 and 4.1), including appropriate error bars (following Cahale 1986).

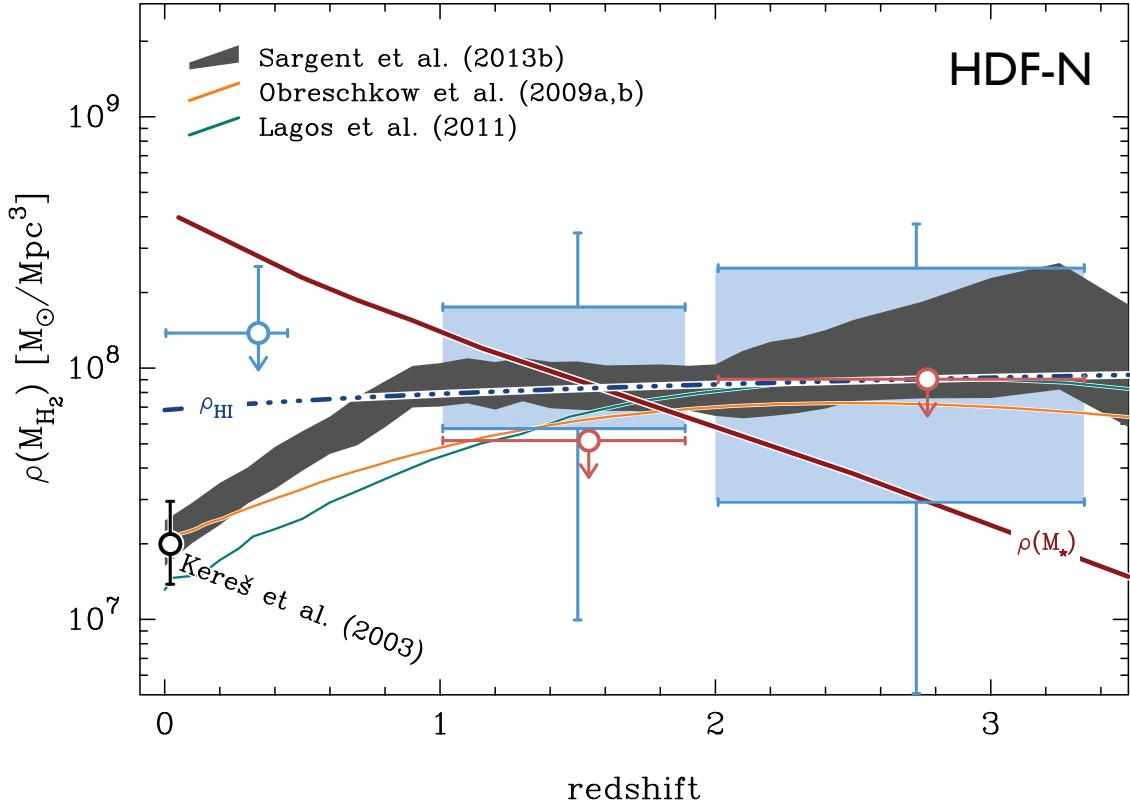


FIG. 5.— The evolution of the cosmic H_2 mass density, $\rho_{H_2}(z)$ based on predictions from semi-analytical cosmological models (Obreschkow et al. 2009a, 2009b, Lagos et al. 2011) as well as the empirical predictions by Sargent et al. (2013b). The latter shows the evolution inferred from the integration of the indirectly inferred molecular gas mass functions underlying the CO luminosity distributions of Fig. 4. The blue-shaded area shows only the contribution of the blind detections (blue-shaded regions in Fig. 4) to $\rho(M_{H_2})$, *not* corrected/extrapolated for a population of undetected sources at lower or higher L'_{CO} . The red upper limit indicates the limit to the gas density contribution strictly for the specific galaxy populations selected via optical spectroscopic redshifts (Sec. 3.1). Our limit in the lowest redshift bin is not very constraining given the small volume probed. For a comparison, the evolution of the cosmic neutral gas mass density (ρ_{HI}) and of the stellar mass density (ρ_{\star}) are also plotted.

TABLE 4
NUMBER OF BLIND CO DETECTIONS AND LIMITING LUMINOSITIES IN SCAN

| line | $\langle z \rangle$ | # ^a | $L'_{\text{CO}}{}^{3\sigma}$ $10^9 \text{ K km s}^{-1} \text{ pc}^2$ | $L'_{\text{CO}(1-0)}{}^{3\sigma}$ $10^9 \text{ K km s}^{-1} \text{ pc}^2$ ^b | density ^c 10^{-3} Mpc^{-3} |
|---------|---------------------|----------------|---|---|--|
| CO(1-0) | 0.338 | 0 | 1.0 | 1.0 | <10.9 |
| CO(2-1) | 1.52 | 1-3 | 5.2 | 6.2 | 0.69-2.10 |
| CO(3-2) | 2.75 | 1-8 | 6.6 | 13.2 | 0.41-3.28 |

^a Number of blind detections in the molecular line scan above our sensitivity limit (next column) as derived in D13 (see Sec 3.2).

^b See Tab. 3 caption for details on conversion from L'_{CO} to $L'_{\text{CO}(1-0)}$.

^c Volume density of sources in redshift bin using column 2 in Tab. 1. In case of no detection (first redshift bin) we assume an upper limit of one source.

based on semi-analytical cosmological models by Lagos et al. (2011) and Obreschkow et al. (2009), both interpolated to our relevant median $\langle z \rangle$ based on their predictions at lower/higher redshift. The luminosities plotted here are computed for the CO(1–0) line (i.e. $L'_{\text{CO}(1-0)}$) and we have converted our higher-J CO luminosities and upper limits to $L'_{\text{CO}(1-0)}$ (see Tab. 3 caption). The CO luminosity function has to date only been directly measured at $z=0$ (see data points by Kereš et al. 2003 in the left panel of Fig. 4).

In order to compare our measurements to these empirically predicted luminosity functions, we need to normalize our number densities in a consistent way. In the literature, the volume densities are typically given in units of sources per Mpc^3 and dex in luminosity ($L'_{\text{CO}(1-0)}$). For our blind detections we define luminosity bins to range from our 3σ limiting luminosity (Tab. 4) to a luminosity that is a factor of 10 higher (i.e., 1 dex). We then count the number of blind detections in this luminosity bin. We have at least two secure CO detections (one in the $z \sim 1.52$ redshift bin, one in the bin with $\langle z \rangle = 2.75$), and potentially up to 11 (3 at $\langle z \rangle = 1.52$, 8 at $\langle z \rangle = 2.75$), if we include all the ‘high-quality’ line candidates in D13 (see Sec. 3.2). The lower limits in the plots are thus from our secure detections. The upper limits represent the case where all line candidates are in fact real. In the limit of low number statistics we adopt the Poisson errors following Gehrels (1986, their tables 1 and 2). We plot the allowed parameter space of our observations as blue-shaded regions in Fig. 4. Our blind detections thus probe the ‘knee’ of the predicted CO luminosity functions.

4.2. Constraints on $\rho_{\text{H}_2}(z)$

We now proceed to convert our constraints on the CO luminosity function to constraints on the cosmic volume density of the molecular gas mass $\rho_{\text{H}_2}(z)$. This is shown in Fig. 5 where we compare our observations to the same models and empirical predictions as discussed in Sec. 4.1 and Fig. 4. For a comparison we also show the evolution of $\rho(M_{\text{HI}})$ based on Bauermeister et al. (2010) and $\rho(M_*)$ based on the compilations in Marchesini et al. (2009) and Fontana et al. (2006).

The blue-shaded area in Fig. 5 (with appropriate error bars) indicates the contribution of our blind CO detections to $\rho_{\text{H}_2}(z)$ from Fig. 4. To translate the observed CO luminosities to H_2 masses we have assumed a galactic H_2 -to-CO conversion factor and BzK excitation (see discussion in D13). In Fig. 5 we do not attempt to correct for sources not detected in our scan at both lower and higher L'_{CO} luminosities, given the unknown shape of the luminosity function. We note though that if we simply scaled up the predicted luminosity functions by Sargent et al. (2013b) so that they are consistent with our observational constraints in Fig. 4, then the values for $\rho_{\text{H}_2}(z)$ would lie above the empirical predictions shown in Fig. 5. This however would imply an overestimate of the number-density of the known population of galaxies.

In Fig. 5 we also show the contribution of the galaxies for which we obtained a stacked upper limit (Sec. 3.1). Like in the case of the blind detections, we do not attempt to correct this measurement for undetected sources at lower (or higher) CO luminosities. The upper limit shown in red color thus simply represents the

contribution of the galaxies for which spectroscopic information is available as discussed in Sec. 3.1 and Fig. 2 and 3.

We conclude that the contribution of *just* our blind detections to the cosmic molecular gas density $\rho_{\text{H}_2}(z)$ already constitute a major contribution to current empirical predictions and models. As a consequence, accounting for the contribution of yet undetected sources (at lower or higher CO luminosities) would give values that lie above the predictions.

5. SUMMARY AND OUTLOOK

Our molecular line scan of the HDF-N (D13) allows us to place first direct ‘blind’ limits on the molecular gas density in ‘normal’ galaxies at high redshift. We have used the rich multiwavelength and spectroscopic database to derive some of the best constraints on CO luminosities in high redshift galaxies to date. We combine our blind CO detections (D13) with stacked CO limits based on galaxies with available spectroscopic redshifts in the HDF-N to give first constraints on the CO luminosity functions and the cosmic evolution of the H_2 mass density $\rho_{\text{H}_2}(z)$ out to redshifts $z \sim 3$ in the HDF-N.

The securely detected sources in our molecular line scan provide significant contributions to the predicted $\rho_{\text{H}_2}(z)$ in the redshift bins $\langle z \rangle \sim 1.5$ and $\langle z \rangle \sim 2.7$. If we were to extrapolate their contribution towards undetected sources at lower and higher CO luminosities we would get $\rho(M_{\text{H}_2})$ values that would exceed predictions (the precise number will depend on the assumed shape of the luminosity function). This in turn would imply that current predictions, e.g., those based on the galaxies’ star formation activity and ‘inverting’ the star formation law, would not account for all the molecular gas that is actually present in galaxies. We note however that the current uncertainties in our precursor study (in particular the current luminosity limits, number of detections, as well as cosmic volume probed) are significant, and that current models can thus not be ruled out given the available data. In addition, the effects of cosmic variance can not be evaluated by just looking at one field. The emerging capabilities of the Atacama Large (Sub-)Millimeter Array (ALMA) with its order-of-magnitude increase in sensitivity will enable similar molecular deep field studies to much deeper levels and larger areas (e.g. Da Cunha et al. 2012, Carilli & Walter 2013). One caveat is that CO may break down as a reliable tracer for H_2 mass in extreme environments, in particular at low metallicities (e.g. Bolatto et al., 2013, Genzel et al. 2012, Schrubba et al. 2011). The sensitivities of our current observations are such that we are only sensitive to gas in galaxies as massive and luminous as L^* , i.e. environments in which the metallicities are not expected to be below solar given the fundamental metallicity relation (Mannucci et al. 2011). Future, much more sensitive, observations of molecular deep fields with ALMA that include measurements of the dust continuum (and thus an independent measure of the mass of the interstellar medium) are essential to (a) further constrain possible metallicity dependences of the CO-to- H_2 conversion factor for a large sample of well-characterized high redshift galaxies and (b) further directly constrain the cosmic evolution of the molecular gas reservoir in galaxies.

We thank the referee for a very helpful and constructive report. FW, DR and EdC acknowledge the Aspen Center for Physics where parts of this manuscript were written. This paper is based on observations with the

IRAM Plateau de Bure Interferometer (PdBI). IRAM is supported by INSU/CNRS (France), MPG (Germany) and IGN (Spain). Support for RD was provided by the DFG priority program 1573 ‘The physics of the interstellar medium’.

REFERENCES

- Barger A.J., Cowie L.L., Wang W.-H., 2008, *ApJ*, 689, 687
 Bauermeister, A., Blitz, L., & Ma, C.-P. 2010, *ApJ*, 717, 323
 Bell, E. F., Zheng, X. Z., Papovich, C., et al. 2007, *ApJ*, 663, 834
 Bolatto, A. D., Wolfire, M., & Leroy, A. K. 2013, arXiv:1301.3498
 Bouwens, R. J., Illingworth, G. D., Oesch, P. A., et al. 2010, *ApJ*, 709, L133
 Carilli, C., & Walter, F. 2013, arXiv:1301.0371
 Cowie, L. L., Barger, A. J., Fomalont, E. B., & Capak, P. 2004, *ApJ*, 603, L69
 da Cunha, E., Walter, F., Decarli, R., et al. 2013, *ApJ*, 765, 9
 Daddi E., et al. 2007, *ApJ*, 670, 156
 Dannerbauer, H., Daddi, E., Riechers, D. A., et al. 2009, *ApJ*, 698, L178
 Decarli, R., Walter, F., et al., *ApJ*, subm. 2013 (D13)
 Dickinson, M., Papovich, C., Ferguson, H. C., & Budavári, T. 2003, *ApJ*, 587, 25
 Dunne, L., Ivison, R. J., Maddox, S., et al. 2009, *MNRAS*, 394, 3
 Fontana, A., Salimbeni, S., Grazian, A., et al. 2006, *A&A*, 459, 745
 Gehrels, N. 1986, *ApJ*, 303, 336
 Ilbert, O., Capak, P., Salvato, M., et al. 2009, *ApJ*, 690, 1236
 Genzel, R., Tacconi, L. J., Combes, F., et al. 2012, *ApJ*, 746, 69
 Grogan, N. A., Kocevski, D. D., Faber, S. M., et al. 2011, *ApJS*, 197, 35
 Hopkins, A. M., & Beacom, J. F. 2006, *ApJ*, 651, 142
 Karim, A., Schinnerer, E., Martínez-Sansigre, A., et al. 2011, *ApJ*, 730, 61
 Keres, D., Yun, M. S., & Young, J. S. 2003, *ApJ*, 582, 659
 Koekemoer, A. M., Faber, S. M., Ferguson, H. C., et al. 2011, *ApJS*, 197, 36
 Lagos, C. D. P., Baugh, C. M., Lacey, C. G., et al. 2011, *MNRAS*, 418, 1649
 Le Fèvre, O., Vettolani, G., Garilli, B., et al. 2005, *A&A*, 439, 845
 Lilly, S. J., Le Fèvre, O., Renzini, A., et al. 2007, *ApJS*, 172, 70
 Marchesini, D., van Dokkum, P. G., Förster Schreiber, N. M., et al. 2009, *ApJ*, 701, 1765
 Mannucci, F., Cresci, G., Maiolino, R., Marconi, A., & Gnerucci, A. 2010, *MNRAS*, 408, 2115
 Newman, J. A., Cooper, M. C., Davis, M., et al. 2012, arXiv:1203.3192
 Obreschkow, D., Heywood, I., Klöckner, H.-R., & Rawlings, S. 2009a, *ApJ*, 702, 1321
 Obreschkow, D., Croton, D., De Lucia, G., Khochfar, S., & Rawlings, S. 2009b, *ApJ*, 698, 1467
 Sargent, M. T., Daddi, E., Béthermin, M., et al. 2013, arXiv:1303.4392
 Sargent et al. 2013b, M. T., et al., in prep.
 Sargent, M. T., Béthermin, M., Daddi, E., & Elbaz, D. 2012, *ApJ*, 747, L31
 Schrubba, A., Leroy, A. K., Walter, F., et al. 2012, *AJ*, 143, 138
 Stark, D. P., Ellis, R. S., Chiu, K., Ouchi, M., & Bunker, A. 2010, *MNRAS*, 408, 1628
 Steidel, C. C., Shapley, A. E., Pettini, M., et al. 2004, *ApJ*, 604, 534
 Steidel, C. C., Erb, D. K., Shapley, A. E., et al. 2010, *ApJ*, 717, 289
 Walter, F., Decarli, R., Carilli, C., et al. 2012, *Nature*, 486, 233
 Williams, R. E., Blacker, B., Dickinson, M., et al. 1996, *AJ*, 112, 1335